AGU PUBLICATIONS

Geochemistry, Geophysics, Geosystems

RESEARCH ARTICLE
10.1002/2017GC007285

Polymorphic Nature of Iron and Degree of Lattice Preferred Orientation Beneath the Earth's Inner Core Boundary

Maurizio Mattesini[1,2], Anatoly B. Belonoshko[3], and Hrvoje Tkalčić[4]

[1]Department of Earth's Physics and Astrophysics, Complutense University of Madrid, Madrid, Spain, [2]Instituto de Geociencias (UCM-CSIC), Facultad de Ciencias Físicas, Madrid, Spain, [3]Condensed Matter Theory, Department of Physics, KTH Royal Institute of Technology, AlbaNova University Center, Stockholm, Sweden, [4]Research School of Earth Sciences, The Australian National University, Canberra, ACT, Australia

Key Points:
- A multiphase lattice-preferred orientation pattern is obtained beneath the Earth's inner core boundary
- The inner core consists of a widespread melting area of low lattice alignment and two confined freezing zones of high crystal ordering
- The cubic iron polymorph governs the physical behavior of the outermost part of the Earth's inner core

Correspondence to:
M. Mattesini,
mmattesi@ucm.es

Citation:
Mattesini, M., Belonoshko, A. B., & Tkalčić, H. (2018). Polymorphic nature of iron and degree of lattice preferred orientation beneath the earth's inner core boundary. *Geochemistry, Geophysics, Geosystems*, *19*, 292–304. https://doi.org/10.1002/2017GC007285

Received 11 OCT 2017
Accepted 2 JAN 2018
Accepted article online 8 JAN 2018
Published online 25 JAN 2018

Abstract Deciphering the polymorphic nature and the degree of iron lattice-preferred orientation in the Earth's inner core holds a key to understanding the present status and evolution of the inner core. A multiphase lattice-preferred orientation pattern is obtained for the top 350 km of the inner core by means of the *ab initio* based *Candy Wrapper Velocity Model* coupled to a Monte Carlo phase discrimination scheme. The achieved geographic distribution of lattice alignment is characterized by two regions of freezing, namely within South America and the Western Central Pacific, that exhibit an uncommon high degree of lattice orientation. In contrast, widespread regions of melting of relatively weak lattice ordering permeate the rest of the inner core. The obtained multiphase lattice-preferred orientation pattern is in line with mantle-constrained geodynamo simulations and allows to setup an ad hoc mineral physics scenario for the complex Earth's inner core. It is found that the cubic phase of iron is the dominating iron polymorph in the outermost part of the inner core.

1. Introduction

The interior structure of the Earth in its simplest approximation is layered in a similar fashion to onion-like spherical shells, and its center represents one of the most inaccessible and enigmatic parts of our planet. The deepest layer is known as the Earth's inner core, a rather small (less than 1% of the entire Earth's volume) spherical, solid body pinpointed exactly at the Earth's center, and made of a pseudomolten iron-nickel (Fe-Ni) alloy. The inner core material is thus subjected to extreme physical conditions, with a temperature similar to the Sun's surface temperature of 6,000 K and a pressure range from 330 to 360 GPa (Dziewonski & Anderson, 1981). It is the Earth's gradual cooling that causes the inner core to grow by solidification of the surrounding melted alloy in the lowermost outer core layer. The release of latent heat and the extraction of impurities into the liquid iron produce buoyant fluid that stirs the outer core and generates the Earth's magnetic field (Braginsky, 1963; Gubbins, 1977; Loper, 1978; Verhoogen, 1961). Apart from a fundamental interest in the Earth's dynamo, the study of the mechanism behind the inner core growing may be crucial to enhance the understanding of the complex heterogeneous isotropic and anisotropic seismic structures of the inner core, which is one of the earliest and long-standing pieces of puzzle that arouse from seismic observations (e.g., Morelli et al., 1986; Shearer, 1994; Shearer & Toy, 1991). Nowadays, it is well accepted that the thermal mantle convection with low velocities (0.1 m/yr), regulates the cooling of the low-viscosity outer core, where rapid flows can exist (10^4 m/yr), thus indirectly setting the speed of inner core growth (0.5 mm/yr). A preferential crystal alignment, i.e., texture, can be established at the time of solidification or may even develop as a result of successive deformation of the solid core material.

The inner core crystallizes from the center outward because the core's melting temperature increases with depth faster than the core geotherm (Jacobs, 1953). The freezing of the outer-core material, basically a melted iron (∼85 wt %)-nickel (∼5 wt %) alloy with ∼10 wt % of light elements (Si, S, O, C, P, H. . .etc.), results in an outward crystallization at a rate that is controlled by the heat extraction from the core by mantle convection. To date, three potential causes of crystal alignment during the solidification of the core material were considered: (i) compressional and tensional deformation due to nonuniform growth of the core (Yoshida et al., 1996), (ii) dendritic solidification (Bergman, 1997), and (iii) crystal alignment due to Maxwell stresses (Buffett & Wenk, 2001; Karato, 1999). According to the first mechanism, solidification of liquid

iron at Inner Core Boundary (ICB) occurs under shear compression across the liquid-solid interface, a process that favors the development of spatially oriented iron microcrystals. Dendritic crystallization instead originates from the supercooled liquid metal *via* fast crystal nucleation. This process leads to relatively small crystal grains displaced in a complex multibranching *tree-like* pattern. The third mechanism considers the possibility that iron crystals nucleated at the ICB region would align according to the local magnetic field lines during sedimentation, providing that grain rotation is faster than sedimentation's velocity. The magnitude of these magnetic effects (Ruban et al., 2013), together with crystal size, heat flow conditions, turbulence, and local spatial orientation of the magnetic field would lead to different and rather complex unit cell orientations (Karato, 1993). All these three mechanisms were so far considered the engine for building texture and assembling a degree of Lattice Preferred Orientation (LPO) in the core material, though the dendritic solidification and the compressional-tensional deformation are mechanisms that are most likely influenced by heat flow variations. Assuming the present-day viscosity regime, strain rates produced by Lorentz forces are perhaps insufficient to sustain texturing in the consolidated inner core material (Lasbleis et al., 2015), even though they can still play a role in the crystallizing process underneath freezing spots.

In this study, we are seeking to answer what drives the lattice ordering in different regions of the inner core by accounting for a precise multiphase iron-solidification pattern at the ICB. This knowledge will provide stronger constraints on the mechanisms that are governing the thermochemical evolution of the core material, which is an essential step forward to understanding the internal dynamics of the Earth's core.

A possible way to accomplish this type of key information is first to rely on a particular thermal heat-flux pattern obtained from dynamical simulations and then working out backward the spatial distribution of iron crystal alignment at ICB. For instance, supposing that the inner core crystallizes dendritically (Bergman et al., 2000, 2005), the resulting growing dendrite pattern at the ICB would be shaped by the local direction and strength of the selected heat flux (Chalmers, 1964). This would yield a heat-flow driven preferred texture that can explain both elastic anisotropy and hemispherical dichotomy of the inner core (Niu & Wen, 2001; Tanaka & Hamaguchi, 1997). Thus, a direct connection between the heat-flux from geodynamic models and the amount of LPO at ICB could be established (Sumita & Olson, 1999). Nevertheless, the main drawback of this approach resides in the choice of the heat-flux pattern, which is rather critical and, overall, not unique, leading to results that are strongly model-dependent. As a matter of fact, three different dynamical models were so far proposed (Table 1). According to the scenario suggested by Aubert et al. (2008), the connection between the lowermost mantle and the inner core induces textural heterogeneity on the core's solidification front. The liquid flow in the outer core is characterized by the presence of cyclones and anticyclones, with the largest cyclone beneath the Southeast Asia. In this model, the heat-flux at the ICB can only be positive, that is outward from the inner to the outer core. The texture of the inner core material corresponding to the areas of fast and slow growth could be characterized by the existence of small and large grains, respectively. Monnereau et al. (2010) and Alboussiére et al. (2010), introduced a second dynamical model scenario where a superadiabatic inner core with a harmonic degree-one thermal heterogeneity induces displacement of core material to maintain its center of mass. Melting on the warmer side (*quasi*-Eastern Hemisphere, *q*-EH) and crystallization on the colder one (*quasi*-Western Hemisphere, *q*-WH) are the postulated mechanisms that operate in removing positive (*q*-EH) and negative (*q*-WH) hemispherical topographies. Texture of the inner core corresponding to the areas of freezing and melting could be then characterized by the existence of large and small grains. Specifically, larger grains are expected to grow in the hotter *q*-EH, while small grains are more likely to form in the colder *q*-WH. Lately, Gubbins et al. (2011)

Table 1
A Summary of the Main Dynamical Scenarios Used to Explain the Observed Seismological Data

Dynamical scenario	Large grains	Small grains	Main spherical harmonic pattern
Aubert et al. (2008)	Pacific (weak heat flow, slow growth)	Southeast Asia (strong heat flow, faster growth)	$Y_{2,2}$
Monnereau et al. (2010) and Alboussière et al. (2010)	*q*-EH (melting)	*q*-WH (freezing)	$Y_{1,1}$
Gubbins et al. (2011)	Pacific (inward heat flow, melting)	Circum-pacific-belt (outward heat flow, freezing)	$Y_{2,2}$

suggested a third model scenario where, unlike the model of Aubert et al. (2008), the heat-flux at ICB can assume both positive and negative sign, thus causing either freezing or melting. The most relevant difference between the model of Monnereau et al. (2010) and Alboussiére et al. (2010) and those of Aubert et al. (2008) and Gubbins et al. (2011), in the context of how regional variations in lattice orientation can develop, lays in dominant harmonic degree-one structure of the former models. A more detailed review of the abovementioned dynamical models can be found in Tkalčić (2015, 2017).

A way to overcome ambiguity in choosing a reference heat-flux model becomes possible by approaching the problem from a slightly different angle. Here, we propose an inside-out view of the heat-flux action, where the *cause-effect* relationship between the known heat-flux (the cause) and the unknown lattice alignment (the effect) is flipped. Our *known* variable is now the LPO spatial distribution at the ICB, whereas the *unknown* magnitude is here denoted by the direction and strength of the heat-flux. The advantage of such a methodology is twofold: (i) the LPO pattern at the ICB can be directly computed from the analysis of seismic data without the need to rely on, a priori, a specific theoretical heat-flux pattern, and (ii) the achieved LPO distribution can be further used to discriminate between different dynamical heat-flux models and, most importantly, impose critical boundary conditions for novel geodynamical simulations.

In the following sections, we first explain how we obtain the geographic distribution and degree of LPO at the ICB by bridging together seismic data with *ab initio* elastic tensors of various iron model phases. We then analyze its implications for a reference heat-flux scenario. We describe the mineral physics mechanism responsible for the heterogeneous seismic structure in the shallow part of the inner core. Velocity of compressional waves is then discussed in terms of a more generalized mineral physic scenario that explicitly takes into account the iron multiphase nature of the Earth's inner core.

2. Data and Methods

With the aim to address the degree of LPO for a set of seismic data, one would ideally select the thermodynamically most stable mineralogical phase of iron at a given depth (beneath the ICB) and then work out the LPO by matching the theoretical and observed travel-times of seismic waves that are probing the inner core. Nonetheless, the *ab initio* thermodynamic stability of the two most likely iron phases for the inner core, namely the body-centered-cubic (*bcc*) and its hexagonal-close-packed form (*hcp*), becomes very similar beneath the ICB (Belonoshko et al., 2003). The two phases are then said to be competitive model systems under the same P,T-conditions, and this hampers the application of the principle of minimum energy in discriminating the two iron polymorphs especially given the uncertainty of amount and composition of light elements. The alternative method that we are here proposing relies on the search for the iron model phase that shows the smallest uncertainty in the theoretical seismic wave velocity. This procedure guarantees the achievement of the most precise LPO pattern beneath the ICB by discriminating the various iron polymorphs on the basis of pure stochastic reasoning.

In the following we describe how the geographical distribution of the iron lattice preferred orientation was achieved at the ICB *via* the *Candy Wrapper Velocity Model* (CWVM) (Mattesini et al., 2013). Such an inner core compressional velocity model connects high-quality inner core-probing seismic data, i.e., the differential travel times of PKPbc and PKIKP waves with a sensitivity down to a maximum of 350 km depth beneath the ICB (Leykam et al., 2010; Tkalčić et al., 2002; Young et al., 2013), together with the elastic constants of different iron polymorphs from *first-principles* molecular dynamics calculations (Mattesini et al., 2010). The CWVM is a multiphase iron model that allows accounting for a complex pseudolocalized anisotropy beneath the ICB. Accordingly, we have considered an inner core picture that is slightly more complex than the two-end-member cases, the large-scale anisotropic structure due to plastic deformation (i.e., a global cylindrical anisotropy; Lincot et al., 2015) from one side and, the perfect stratification regime (i.e., a very localized anisotropy) from the other. The CWVM is able to sustain a core configuration that is halfway, where a finer conglomerate of complex multiphase domains builds up the outermost inner core (Mattesini et al., 2013; Tkalčić, 2010). Among various iron model phases, the CWVM incorporates the cubic structure with [111] crystal direction parallel to the Earth's spinning axis, which is known as the cylindrically averaged body-centered-cubic ($\overline{bcc}$) phase. According to the cylindrically anisotropic model (Song, 1997; Stixrude & Cohen, 1995; Thomsen, 1986), the polar-equatorial velocity difference for $\overline{bcc}$ is 2.64%, while for the hexagonal-close-packed aggregates such variation amounts to 1.95% (Mattesini et al., 2010). Therefore, differences in seismic wave velocities along the polar and equatorial paths are significantly dissimilar for the two types of

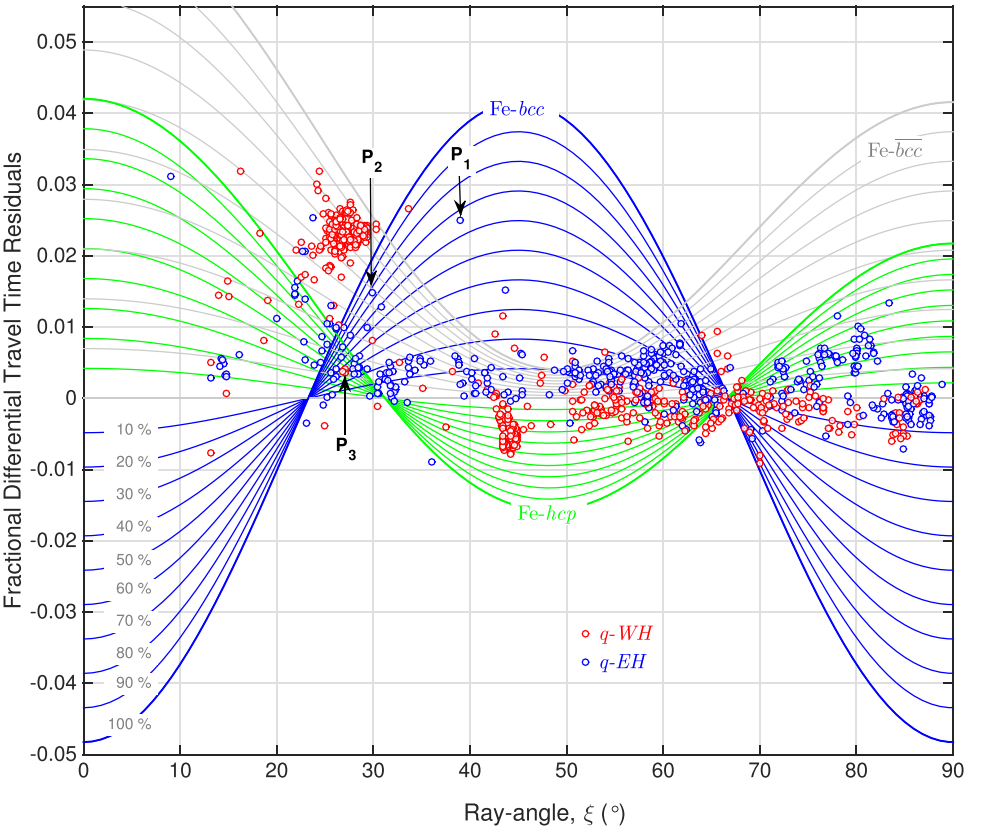

Figure 1. Fractional differential travel-time residuals versus ray-angle for the *Candy Wrapper Velocity Model*. Solid lines are the different LPO percentages (0–100%), while open circles are the employed seismic data points, red for the *quasi*-western hemisphere, and blue for the *quasi*-eastern hemisphere according to the definition of hemispherical structure outlined in Tanaka and Hamaguchi (1997). Blue, green, and gray lines are the theoretical velocity curves from *first-principles* calculations. Modified from Figure 4b of Mattesini et al. (2013).

aggregates, unlike those presented in Figure 3 of Romanowicz et al. (2016). It is certainly worth remarking that the cylindrically averaged cubic iron is the mineral physics model with the largest anisotropy in the compressional wave velocity (V_p) (Mattesini et al., 2010).

As V_p in the CWVM depends on both ray-angle (ξ) and percentage of LPO (Figure 1), it becomes possible to obtain an LPO distribution pattern for a specific iron model phase, such as for the bare Fe-*bcc*, its cylindrically averaged form ($Fe-\overline{bcc}$) and the Fe-*hcp* system. The main difference between the bare *bcc* and its cylindrical arrangement resides on the direction of the fast velocity axis, i.e., the main diagonal of the unit cell. While the bare *bcc* has its fast velocity axis at 54.74° from the crystallographic *c*-axis, the main diagonal of the cylindrically averaged *bcc* is parallel to the vertical *c*-axis direction. Hence, the symmetry of the elastic tensor changes from cubic (Fe-*bcc*) to hexagonal ($Fe-\overline{bcc}$).

We then considered the LPO as a numerical coefficient that, for a selected crystal phase and a given ray-angle, allow matching the theoretical velocity curve to a seismically observed travel time residual. The LPO variable assumes values between 0 (0% of lattice alignment) and 1 (100% of lattice ordering), and can be analytically computed from a modified form of the CWVM (Mattesini et al., 2013). The worked out mathematical relationship for LPO is shown below for a generic iron model phase (*phase* = *bcc*, $\overline{bcc}$ or *hcp)*:

$$LPO^{(Fe-phase)} = \frac{FDTTR(\xi,\theta)\cdot V_{po}^{(Fe-phase)}}{\left[V_p(\xi)^{(Fe-phase)} - V_{po}^{(Fe-phase)}\right]}, \quad (1)$$

where the $V_p(\xi)^{(Fe-phase)}$ term stands for the *ab initio* computed sound velocity at a specific ray-angle value (ξ), $V_{po}^{(Fe-phase)}$ is the reference polycrystalline compressional velocity, and FDTTR(ξ,θ) represents the Fractional Differential Travel-Time Residual for a particular ξ and azimuthal-angle (θ):

$$FDTTR(\xi,\theta)=\frac{\left[t(\Delta,\xi,\theta)^{obs}_{PKPbc}-t(\Delta,\xi,\theta)^{obs}_{PKIKP}\right]-\left[t(\Delta)^{ak135}_{PKPbc}-t(\Delta)^{ak135}_{PKIKP}\right]}{t^{ic}(\Delta)^{ak135}_{PKIKP}} \quad (2)$$

For a given epicentral distance (Δ), the model assumes that the observed PKPbc and PKIKP differential travel times $\left[t(\Delta,\xi,\theta)^{obs}_{PKPbc}-t(\Delta,\xi,\theta)^{obs}_{PKIKP}\right]$ are minimally affected by the Earth's structure outside the inner core due to close proximity of PKPbc and PKIKP ray paths. The Hill's averaging method (Hill, 1952) for both bulk and shear moduli was applied to obtain the reference P-wave velocity propagation in a polycrystalline media $\left[V_{po}^{(Fe-phase)}\right]$, whereas the spherically symmetric Earth's model *ak135* (Kennett et al., 1995) was used to compute theoretical differential travel-times $\left[t(\Delta)^{ak135}_{PKPbc}-t(\Delta)^{ak135}_{PKIKP}\right]$ and the time a PKIKP wave stays inside the inner-core, $t^{ic}(\Delta)^{ak135}_{PKIKP}$. The advantage of working with the dimensionless quantity FDTTR(ξ,θ) resides on the fact that we can now operate within a more simple travel-time-ray-angle configuration space, without accounting for by variations in the epicentral distance.

By applying equation (1), it is thus possible to associate an LPO value to every single seismic data point accounted so far in the CWVM of Figure 1. We note, however, that such a straightforward procedure can only be applied when the selected data point is underlined by a single theoretical velocity curve, just as indicated by the point P_1 in Figure 1. When more than one iron model is able to match the same FDTTR value (see for instance points P_2 and P_3 in Figure 1), then a more complex procedure must be adopted. In these cases, we make use of the Monte Carlo (MC) sampling technique to monitor the statistical error propagation in the *first-principles*-computed sound velocities so as to discriminate between two or more theoretical curves that can potentially describe the same seismic data point. Particularly, we examine how the systematic errors from *ab initio* total energy calculations are propagating inside the averaging formulas used to obtain sound velocities. Note that, contrary to the work of Lincot et al. (2015), where the MC method was used to freely span among all possible lattice orientations, the MC sampling here is applied to differentiate between several *frozen* model phases, whose crystal orientations were initially set by the CWVM. Therefore, in this study, the MC scheme is applied just after a search for the preferred lattice orientations, allowing to select the phase that best describes the observed FDTTR. The advantage of such a constrained searching route relies on the fact that the employed iron models are allowed to keep the same orientation constraints found earlier through the CWVM. This is a way of fulfilling the minimal misfit condition (Mattesini et al., 2013) in the seismic data and, to save important physical properties that are intrinsic to certain iron models. For instance, the two preferential orientations captured earlier by the CWVM for the cubic structured iron polymorph (*bcc* and $\overline{bcc}$) might be a sign of a specific response function to magnetic susceptibility during lattice alignment (Ruban et al., 2013). Thus, a set of important physical information can be saved during the entire modeling sequence, instead of being lost in an unconstrained MC procedure.

For clarity, we show the details of our technique when applied to a simple test case, the point P_2 labeled in Figure 1, where the FDTTR value can be equally accounted for by the sound velocity curve of Fe-$\overline{bcc}$ with an LPO of 60% or by the bare Fe-*bcc* with and LPO of 80%. In order to distinguish between the two iron models, we first let vary the values of the computed *ab initio* elastic constants c_{ij} (Mattesini et al., 2013) by using a normal distribution of errors, as shown in the following equation:

$$c_{ij}^{(k)}=c_{ij}+\Delta_e\cdot rand^{(k)} \quad (3)$$

where $\Delta_e = 5$ GPa is the absolute maximum error and $rand^{(k)}$ is the k^{th}-normally distributed pseudorandom number spanning the interval [–1, +1]. Therefore, after having generated $N = 10^4$ random numbers ($k=1\cdots N$) for each c_{ij} we obtain a set of normally distributed elastic constants, which are finally used to compute the following distribution of compressional velocities (Auld, 1973; Thomsen, 1986):

$$V_p^{bcc}(\xi)^{(k)}=(2\rho)^{-\frac{1}{2}}\cdot\left\{c_{11}^{(k)}+c_{44}^{(k)}+\left[\left(c_{11}^{(k)}-c_{44}^{(k)}\right)^2\cos^2(2\xi)+\left(c_{12}^{(k)}-c_{44}^{(k)}\right)^2\sin^2(2\xi)\right]^{\frac{1}{2}}\right\}^{\frac{1}{2}} \quad (4)$$

$$V_p^{\overline{bcc}}(\xi)^{(k)}=\rho^{-1}\cdot\left[c_{11}^{(k)}+\left(4c_{44}^{(k)}+2c_{13}^{(k)}-2c_{11}^{(k)}\right)\cos^2(\xi)+\left(c_{33}^{(k)}+c_{11}^{(k)}-4c_{44}^{(k)}-2c_{13}^{(k)}\right)\cos^4(\xi)\right]^{\frac{1}{2}} \quad (5)$$

By knowing the density (ρ) of the model phase *via ab initio* calculations, the above scheme lends itself to a possibility to monitor how an error Δ_e generated in the computation of c_{ij} propagates and affects the

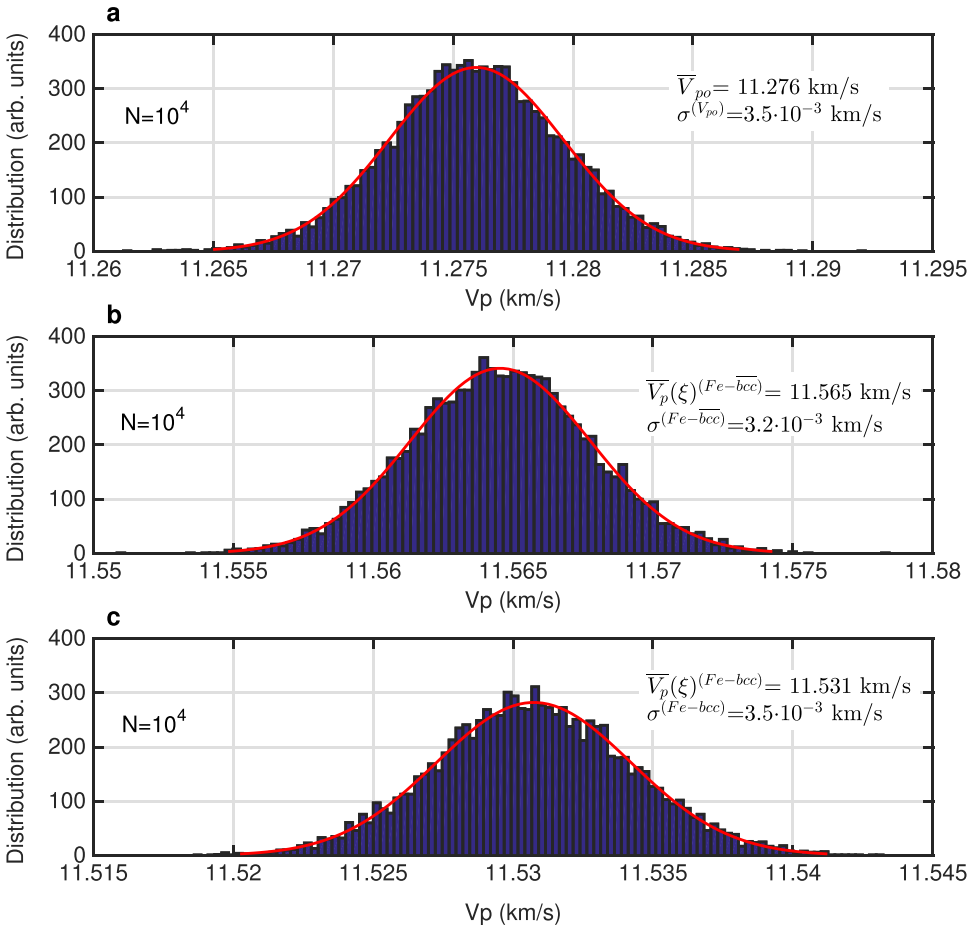

Figure 2. Compressional velocities obtained by Monte Carlo sampling (N = 10^4 points) applied to the test point P_2 from Figure 1 ($\xi = 29.87°$ and FDTTR = 1.48×10^{-2}). The red lines are the best curve fits to the histograms. (top: a) Refers to the cubic polycrystalline model, (middle: b) a cylindrically averaged *bcc* iron, and (lower: c) the bare *bcc* iron.

theoretical velocity curves shown in Figure 1. The achieved histograms of longitudinal velocities are shown in Figure 2 for an averaged polycrystalline iron material (Figure 2a) and for the *bcc* model phases (bare and cylindrically averaged), respectively (Figures 2b and 2c). By inspecting the width of the Gaussian distribution, we are now able to choose the iron model that best describes the observed seismic data point. Since for the specific point P_2 the Fe-$\overline{bcc}$ model shows the lowest standard deviation (σ), an LPO percentage can be analytically assigned via equation (1) by using the most probable $\overline{V}_p(\xi)^{(Fe-\overline{bcc})}$ and $\overline{V}_{po}$ values. The latter numbers correspond to the maxima in the curves fitting of the histograms shown in Figure 2. Using this procedure, the P_2 point can finally be assigned to the Fe-$\overline{bcc}$ model phase with 60% of lattice ordering. The same kind of statistical approach can be further applied to the more complicated test case P_3 of Figure 1, where three different types of velocity curves can, in principle, account for the same seismic data point.

From a more systematic application of the above procedure it was possible to assign each FDTTR point to a specific iron model and to a characteristic degree of LPO. Among the 1,058 seismic data points that were considered in this work, 58.8% were uniquely assigned to a single model phase (i.e., 14.3% to *bcc*, 23.4% to *hcp*, and 21.1% to $\overline{bcc}$) without the need of applying the aforementioned statistical discrimination scheme. However, for the remaining 41.2% of data, the Monte Carlo method was used to discern in between two (38.6%) or three (2.6%) possible overlapping iron models. Figure 1 shows that there are few points (22) with negative FDTTRs at ray-angles between 20°–30° and 60°–70° which are escaping from the CWVM. Because we only contemplate the existence of a positive LPO value, those points were not considered in our procedure and left their LPO unassigned. As a general tendency, we found that the cylindrically averaged Fe$-\overline{bcc}$ system is generally preferred over the other iron models (i.e., it always shows the lowest standard deviation), except in the ray-angle interval between 40° and 50°, where the two cubic models have very similar σ values (Figure 3).

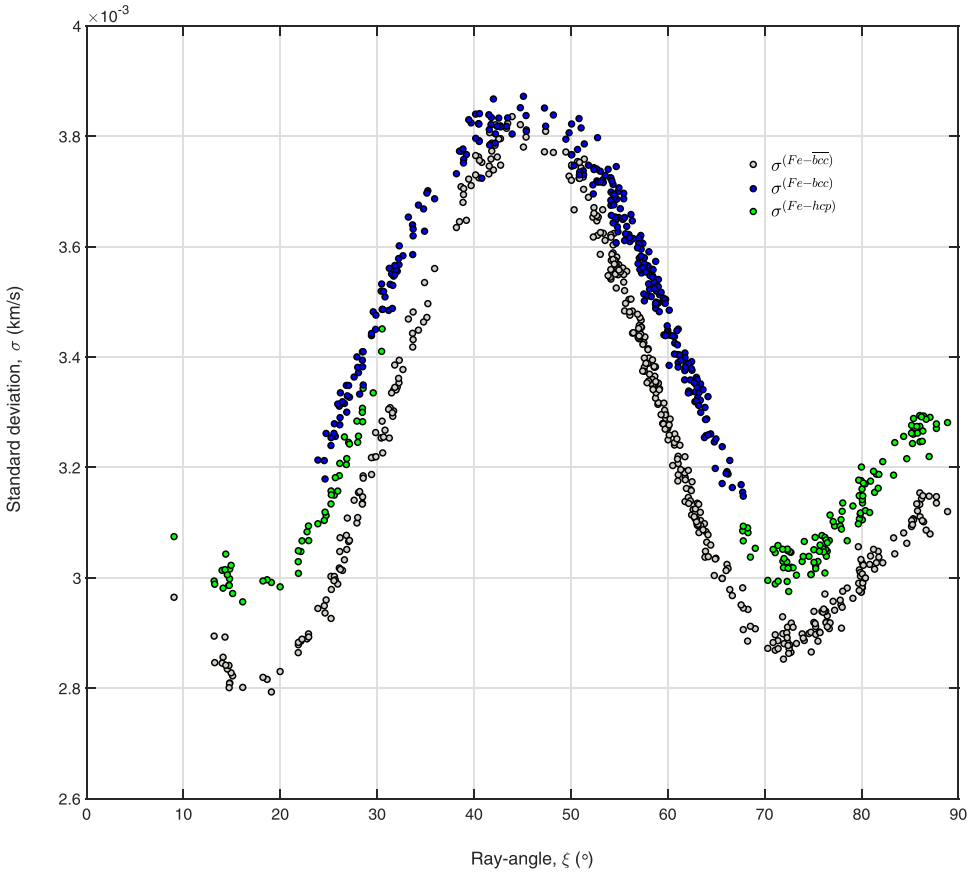

Figure 3. Standard deviation versus ray-angle after Monte Carlo calculations (N = 10^4 points) for the entire set of seismic data points considered in the CWVM. Test calculations using Δ_e up to 20 GPa were carried out without observing significant changes in the results shown in this figure.

The outcome of such a new methodology is in line with previous findings (Mattesini et al., 2010, 2013), where the cylindrically averaged Fe−$\overline{bcc}$ model was found to be the dominating iron phase in the shallow part of the inner core. The featured procedure simultaneously allows carrying out a crystal phase differentiation and a lattice preferred-orientation analysis for the principal iron phases at the Earth's inner core conditions. This provides a basis for working out a multiphase LPO pattern at the ICB, which has a special meaning in addressing the entangled physical behavior of the Earth's inner core.

3. Results and Discussion

A deep insight into the mechanism for lattice alignment in the inner core can be achieved by discerning the spatial distribution of LPO at the ICB. As discussed in the previous section, such important mineral physics inference can be indirectly made from travel time residuals of seismic waves that are probing the inner core along different spatial directions. The achieved iron LPO pattern is shown in Figure 4 and consists of two rather well-confined areas with a high degree of lattice alignment (more than 40%), located beneath the radially projected South America and the Western Central Pacific regions. Their geographic positions are in good agreement with the initial boundary conditions in constrained geodynamo simulations, where the effect of mantle inhomogeneity on heat flow through the ICB was explicitly taken into account (e.g., Gubbins et al., 2011). The two high LPO zones correspond to strong heat flux outward the ICB, where a localized freezing of the core material is taking place. Therefore, the achieved LPO map distribution seems to mirror the heat flux pattern on ICB, which is in turn imposed by the temperature profile at the Core Mantle Boundary (CMB).

If the heat flow across the ICB is governed by the distribution of heterogeneities in the lowermost mantle through quasistationary flows in the outer core (Gubbins et al., 2011), it is possible that

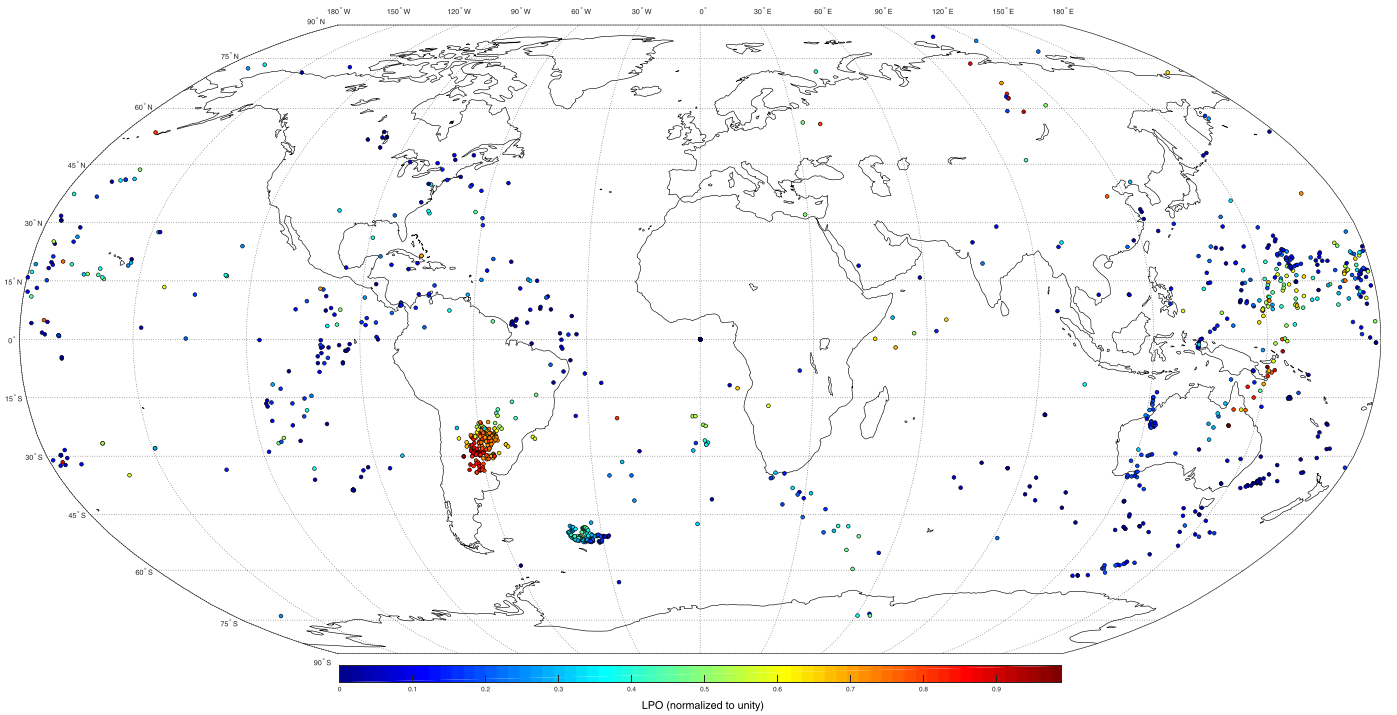

Figure 4. The LPO pattern at the ICB *via* the *Candy Wrapper Velocity Model* coupled to a Monte Carlo phase discrimination scheme for the three iron model phases. The concentration of green/yellow/orange/red-filled circles indicates the localized regions within South America and the Western Central Pacific with a remarkable (>40%) degree of LPO. Latitude and longitude here refer to the ICB piercing entrance of PKIKP waves. Coastlines were radially projected onto the ICB surface to guide the eye. The reported LPO values were computed within a maximum error of $\pm 10\%$ by assuming a systematic uncertainty of the order of $\pm 10^{-3}$ (dimensionless) in the FDTTR values.

seismologically detected multiscale heterogeneities in the lowermost mantle (Tkalčić et al., 2015) can complicate the iron crystallization pattern at ICB. This complex pattern has not yet been fully revealed by the seismological probes, but the recently observed regional variation in compressional velocity (Huang et al., 2015; Wu & Irving, 2017; Yee et al., 2014) and attenuation (Attanayake et al., 2014; Iritani et al., 2014; Pejić et al., 2017) suggest more wide-spread complexity that yet has to be fully mapped and understood. According to the scenario envisaged by the constrained geodynamic simulations, the regional melting and freezing mechanism of the core material provides itself a cause for seismic anomalies in the inner core. Areas of freezing will be made of layers of recently formed (young) and unconsolidated material, where the crystal alignment is more favorable. In such conditions, if the axis along which crystals are oriented corresponds to a fast velocity direction, then these regions would be compatible with a high velocity zone, as already pointed out (Mattesini et al., 2013). Zones of melting instead, which embody the majority of the ICB, will consist of a precompressed (old) core material with a less marked crystal alignment pattern. A finer and by far more complex variation in P-wave velocity at ICB can be further attributed to compositional modification of the inner core material (i.e., different iron polymorphs and amount of light elements) and to changes in its rheological properties (texture, grain size, defects, etc.).

As shown in Table 1, various geodynamical simulations testing the core-mantle boundary effects envisage a grain size difference between the two hemispheres, with larger grains at the central Pacific region (Aubert et al., 2008; Gubbins et al., 2011). It is acknowledged, however, that such a specific grain size modulation is not strictly required by these models (Tkalčić, 2015). The convective translational model (Alboussiére et al., 2010; Monnereau et al., 2010) predicts even larger longitudinal grain size differences between the two hemispheres but, its interpretation from scattering still remains challenging (Attanayake et al., 2014). Indeed, a number of thermodynamic calculations are not sustaining such a large grain size difference across the inner core (Bergman, 1998; Bergman et al., 2010; Buffett, 1997; Deguen et al., 2007; Yoshida et al., 1996). Therefore, because of the shortcoming physical support to any precise grain size

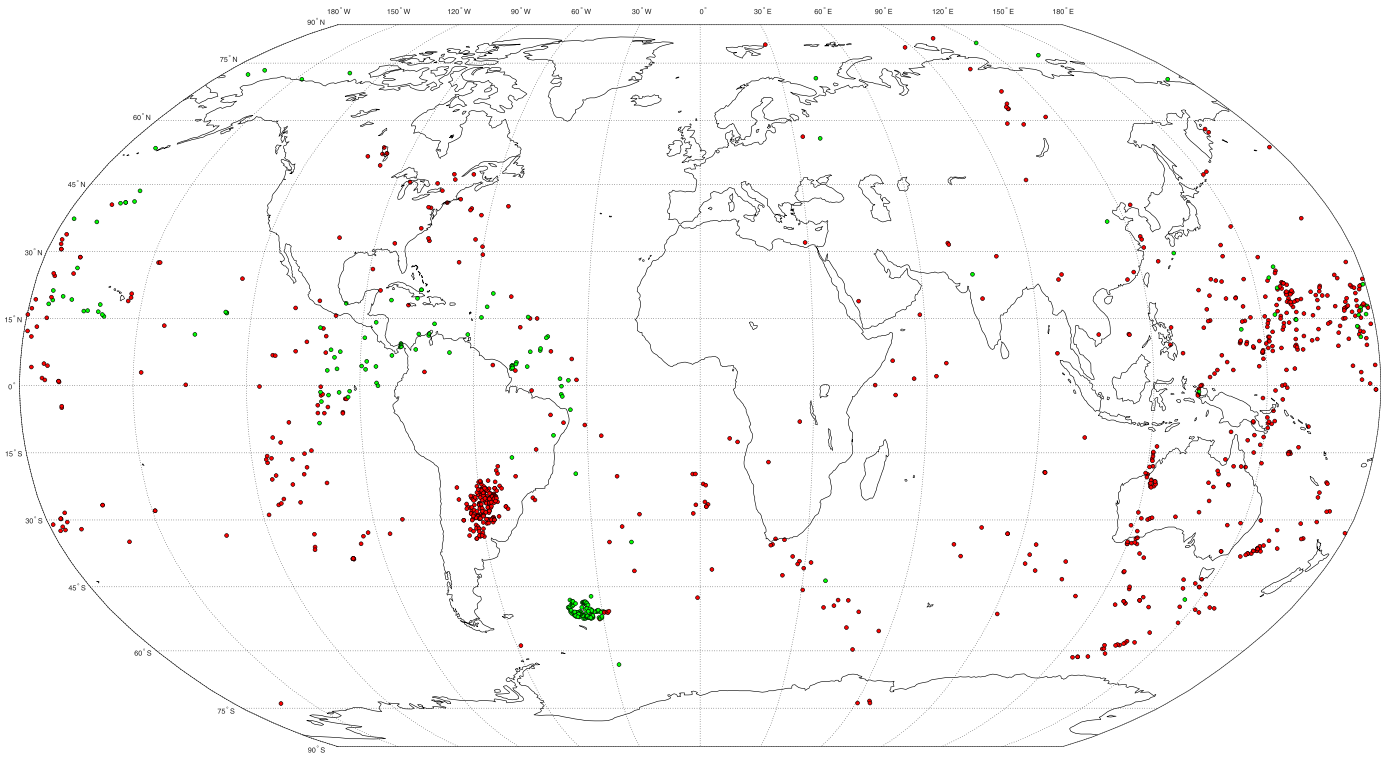

Figure 5. Red circles represent iron *bcc* (either in the bare or in the cylindrically averaged form), while green ones refer to the *hcp* phase.

distribution at ICB, we hereby do not assume a priori any highly constrained dependence on grain size variation at ICB and simply consider that regions of melting will likely contain larger grains than those beneath freezing zones.

By knowing that structure and properties of a crystalline material are closely related to each other, the elasticity of the inner core, its seismic response, density, heat capacity and heat conductivity essentially depend on the phase diagram of iron at core conditions. Thus, to shed light on the specific iron phase distribution at ICB we made use of the CWVM through the stochastic discrimination criterion introduced in section 2. The outcome of such a working technique is shown in Figure 5, where each seismic data point was assigned to a precise type of iron polymorph. The complex mineralogical distribution of iron *bcc* and *hcp* identified in Figure 5 points to a zone-specific physical behavior of the core material that varies in accordance to the different areas probed by the propagating seismic rays. Worth noting is that the achieved mineralogical pattern provides another indirect evidence for *bcc* iron stability at the core conditions (Belonoshko et al., 2003) and plays a key role in addressing regional variations for wave velocity. The South America and the Western Central Pacific freezing zones can be ascribed to the *bcc* polymorph, which is an intrinsically fast (Mattesini et al., 2013) and a remarkably anisotropic iron phase (Mattesini et al., 2013) with a nonvanishing magnetic susceptibility at core conditions (Ruban et al., 2013).

Nowadays, it is well accepted that crystal defects as stacking faults, twin boundaries and dislocations are common in solid iron and can contribute to texture formation in all types of iron polymorphs. However, as recently demonstrated by Belonoshko et al. (2017), *bcc* iron is the only phase that holds an efficient atomic diffusion process inside its crystal lattice. This type of self-diffusion mechanism, which takes place along the [110] directions of the cubic lattice, might play a crucial role during texturing of *bcc* iron. Although a multiscale modeling approach is required to draw any precise conclusion about texture formation in the cubic iron, it is worth noting that such a distinctive atomic diffusion mechanism does not exist for the *hcp* phase. The highly dissipative atomic motion in iron *bcc* could be further responsible for an uncommon (e.g., higher) seismic wave attenuation response of the cubic iron with respect to the hexagonal phase. As such, the wide distribution area disclosed by the cubic phases at ICB, with a special extension on the eastern hemisphere (Figure 5), can itself explain the seismically observed hemispherical velocity variations (Mattesini et al., 2010; Niu & Wen, 2001;

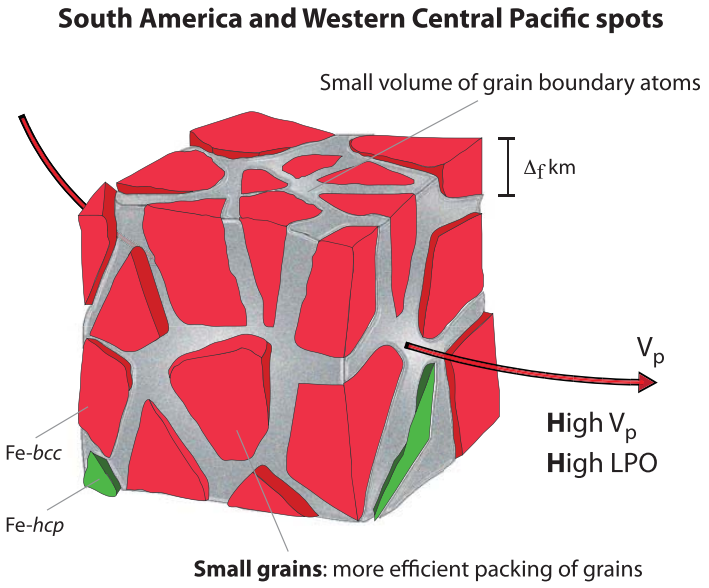

Figure 6. Schematic representation of the inner core material beneath the freezing regions (i.e., an outward heat flux) of the South America and the Western Central Pacific spots. Thickness of the relatively small grains in a freezing-like environment is measured by Δ_f (km). Gray zones represent the surrounding boundary atoms (i.e., surface atoms with higher internal energy than bulk atoms) that are separating pure grains.

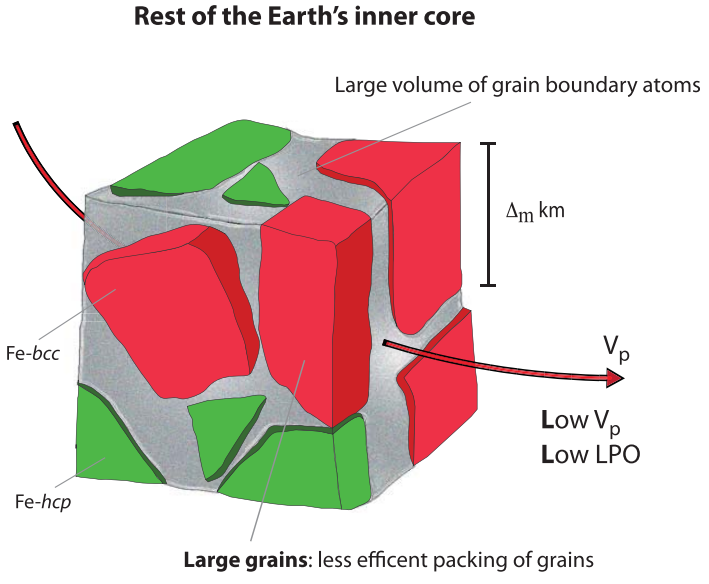

Figure 7. Schematic illustration of the inner core material beneath the widespread melting-like region of the ICB. Larger grains ($\Delta_m \gg \Delta_f$) are assumed to develop beneath an inward heat flux. As shown in Figure 5, the amount of *hcp* grains (green blocks) is maximized beneath the Central America region and minimized when moving toward the eastern hemisphere. The subscripts of Δ indicate either melting-(m) or freezing-like (f) conditions.

Tanaka & Hamaguchi, 1997), and might be also responsible for the complex attenuation pattern found in recent studies (Attanayake et al., 2014; Iritani et al., 2014; Pejić et al., 2017).

In light of these considerations, we hereby propose a common mineral physics scenario for the South America and the Western Central Pacific spots and a different one for the rest of the inner core. As commented earlier, the localized South America and the Western Central Pacific regions are distinguished by a freezing-like core material consisting of relatively well-packed small grains of cubic phase with a remarkable high degree of LPO. A simplified sketch of such a core-type material is shown in Figure 6. The large degree of lattice ordering beneath these zones can be justified by the presence of a strong outward heat flux that can efficiently texture the cubic iron lattice. Because of the high degree of lattice alignment, seismic anisotropy is also expected to be remarkably high under these areas. However, due to the limited ray-angle probing window we could not clearly address this property. The rest of the inner core is marked by a rather extensive melting-like region with a low level of LPO (Figure 4). Such a type of core material is thus characterized by larger grains made of an admixture of both hexagonal and cubic phase (Figure 7). As illustrated in Figure 5, *bcc* iron dominates the outermost part of the inner core except for the region beneath the Central America. It is in this region where the presence of the slower *hcp* polymorph is maximized, providing a low velocity zone for compressional waves.

It is worth remarking that the most salient freezing-like heat flux features foreseen in the dynamic model of Gubbins et al. (2011) were here reproduced in the LPO pattern of Figure 4. However, a finer and overall spatially more distributed seismic sampling of the inner core is highly required in order to clearly discriminate between different geodynamic settings. Addressing whether the spherical harmonic development of the LPO map (not shown here) is dominated by the same $m = 1$ pattern of the geodynamical model of Monnereau et al. (2010) and Alboussiére et al. (2010), or instead favors a spherical harmonic degree-two of Aubert et al. (2008) and Gubbins et al. (2011) (or even higher degrees), remains a complicated task as long as sparseness in the seismic data is not mitigated by the introduction of new observations.

It should be noted that, although the accomplished LPO distribution was developed from seismic data with a marked degree-one heterogeneity in isotropic velocity (see Figure 4b in Mattesini et al., 2013; Tkalčić et al., 2002), it is not trivial to expect the same kind of degree-one pattern to be reflected into the geographic distribution of LPO. In principle, similar seismic travel-time residuals can be either described by high or low degree of crystal alignment depending on the probing ray-angle value. And, this is a direct consequence of the sinusoidal form of the theoretical velocity functions that constitute the CWVM of Figure 1. We remark that the removal of the rather controversial South Sandwich Island (SSI) data, which could carry a strong mantle biased signal either from the SSI subduction slab and/or from the Alaskan slab side (Romanowicz et al., 2003; Tkalčić, 2010), do not qualitatively modify the resulting LPO distribution at the ICB. As a matter of fact, the SSI-Alaska paths are characterized by strong FDTTRs and small ray-angles that basically enlarge and reinforce the South America spot shown in Figures 4 and 5.

4. Conclusions

We show that rheological properties alone are insufficient to explain the seismically observed physical properties of the Earth's inner core. An important weight must be given to the mineralogical nature of the inner core material in order to reconcile modeling and seismic observations. By means of the *Candy Wrapper Velocity Model* and a Monte Carlo sampling phase-discrimination methodology (CWVM-MC) we demonstrate the existence of a complex polymorphic nature of iron and degree of lattice preferred orientation of the inner core material beneath the ICB. The top 350 km of the inner core is characterized by a widespread melting-like region with a rather low level of LPO, while only two very localized regions, namely the South America and Western Central Pacific spots exhibit a unique freezing-like behavior with an uncommon high degree of LPO. The latter zones are crafted by small grains of *bcc* iron, whereas areas of melting are instead composed by larger grains of a more convoluted admixture of cubic and hexagonal polymorphs. The geographic positions of the South America and the Western Central Pacific areas pair fairly well with those of the positive heat flux features found in mantle-constrained geodynamic modeling. This finding strongly reinforces the idea that these areas correspond to strong directional freezing, where an outward heat flux can easily texture and align the cubic iron polymorph. A plausible explanation to such a unique and complex polymorphic pattern and LPO distribution could rely on the subtle and very localized temperature perturbations (10^{-4}–10^{-3} K; Jones, 2000) along the ICB, which could determine the inner core growth rate, its mineralogical composition, grain size and the degree of lattice alignment. Due to the complex coupling between outer core convection and heat extraction pattern at the CMB, small and entangled temperature differences can be left imprinted on the growing inner core surface, and hence mirrored into the LPO pattern at ICB.

The inferred LPO geographical distribution might be used as a possible boundary condition on the ICB for novel dynamo simulations. As a matter of fact, geodynamic models could explain ICB anomalies if one imposes a fixed buoyancy flux having a certain LPO distribution and, then attempt to reproduce the various CMB properties (Aubert et al., 2008, 2013; Olson & Deguen, 2012). Assuming an average inner core growing rate of 5×10^{-7} km/yr (Labrosse et al., 2001) and a maximum probing depth of seismic data of 350 km, we might approximately set the age of the investigated inner core layer to 700 Myr. This clearly bounds the proposed iron LPO arrangement to the younger and shallower inner core part. Thus, we do not exclude a priori that at deeper depths there might be evidences for ancient crystallization patterns with significantly different structures. As such, the inner core dynamics might have changed its characteristic during the Earth's lifetime (Turcotte & Schubert, 2002), moving from an initially more convection-type regime (i.e., lower viscosity range) to a translation-type for the present-day higher inner core viscosity (Mizzon & Monnereau, 2013).

Finally, in view of the recently discovered self-diffusion atomic stabilization process for the cubic iron phase (Belonoshko et al., 2017), we contemplate the possible existence of a fourth type lattice ordering mechanism that might operate inside the Earth's inner core. Such a possibility will be more appropriately investigated elsewhere.

Acknowledgments
Maurizio Mattesini acknowledges financial support by the Spanish Ministry of Economy, Industry and Competitiveness (CGL2013–41860-P and CGL2017–86070-R), and by the BBVA Foundation under the "I convocatoria de Ayudas Fundación BBVA a Investigadores, Innovadores y Creadores Culturales" (PR14 CMA10). A.B.B. was supported by the Swedish Scientific Council (grant 2017-03744 Physics of the Earth's Core). There are no new seismic data in this publication.

References

Alboussiére, T., Deguen, R., & Melzani, M. (2010). Melting induced stratification above Earth's inner core due to convective translation. *Nature*, *466*, 744–747. https://doi.org/10.1038/nature09257

Attanayake, J., Cormier, V. F., & de Silva, S. M. (2014). Uppermost inner core seismic structure: New insights from body waveform inversion. *Earth and Planetary Science Letters*, *385*, 49–58. https://doi.org/10.1016/j.epsl.2013.10.025

Aubert, J., Amit, H., Hulot, G., & Olson, P. (2008). Thermochemical flows couple the Earth's inner core growth to mantle heterogeneity. *Nature*, *454*(7205), 758–761. https://doi.org/10.1038/nature07109

Aubert, J., Finlay, C. C., & Fournier, A. (2013). Bottom-up control of geomagnetic secular variation by the Earth's inner core. *Nature*, *502*(7470), 219–222. https://doi.org/10.1038/nature12574

Auld, B. A. (1973). *Acoustic fields and waves in solids* (Vol. 1). New York, NY: John Wiley & Sons Inc.

Belonoshko, A. B., Ahuja, R., & Johansson, B. (2003). Stability of the body-centred-cubic phase of iron in the Earth's inner core. *Nature*, *424*(6952), 1032–1034. https://doi.org/10.1038/nature01954

Belonoshko, A. B., Lukinov, T., Fu, J., Zhao, J., Davis, S., & Simak, S. I. (2017). Stabilization of body-centred cubic iron under inner-core conditions. *Nature Geoscience*, *10*(4), 312–318. https://doi.org/10.1038/ngeo2892

Bergman, M. I. (1997). Measurements of elastic anisotropy due to solidification texturing and the implications for the Earth's inner core. *Nature*, *389*(6649), 412–412. https://doi.org/10.1038/38786

Bergman, M. I. (1998). Estimates of the Earth's inner core grain size. *Geophysical Research Letters*, *25*(10), 1593–1596. https://doi.org/10.1029/98GL01239

Bergman, M. I., Giersch, L., Hinczewski, M., & Izzo, V. (2000). Elastic and attenuation anisotropy in directionally solidified (hcp) zinc, and the seismic anisotropy in the Earth's inner core. *Physics of the Earth and Planetary Interiors*, *117*(1–4), 139–151. https://doi.org/10.1016/S0031-9201(99)00093-X

Bergman, M. I., Lewis, D. J., Myint, I. H., Slivka, L., Karato, S.-I., & Abreu, A. (2010). Grain growth and loss of texture during annealing of alloys, and the translation of Earth's inner core. *Geophysical Research Letters*, *37*, L22313. https://doi.org/10.1029/2010GL045103

Bergman, M. I., MacLeod-Silberstein, M., Haskel, M., Chandler, B., & Akpan, N. (2005). A laboratory model for solidification of Earth's core. *Physics of the Earth and Planetary Interiors*, *153*(1–3), 150–164. https://doi.org/10.1016/j.pepi.2005.03.016

Braginsky, S. (1963). Structure of the F layer and reasons for convection in the Earth's core. *Doklady Akademi Nauk SSSR English Translation*, *149*, 1311–1314.

Buffett, B. A. (1997). Geodynamic estimates of the viscosity of the Earth's inner core. *Nature*, *388*(6642), 571–573. https://doi.org/10.1038/41534

Buffett, B. A., & Wenk, H. R. (2001). Texturing of the Earth's inner core by Maxwell stresses. *Nature*, *413*(6851), 60–63. https://doi.org/10.1038/35092543

Chalmers, B. (1964). *Principles of solidification*. New York, NY: John Wiley & Sons.

Deguen, R., Alboussière, T., & Brito, D. (2007). On the existence and structure of a mush at the inner core boundary of the Earth. *Physics of the Earth and Planetary Interiors*, *164*(1–2), 36–49. https://doi.org/10.1016/j.pepi.2007.05.003

Dziewonski, A. M., & Anderson, D. L. (1981). Preliminary reference Earth model. *Physics of the Earth and Planetary Interiors*, *25*(4), 297–356. https://doi.org/10.1016/0031-9201(81)90046-7

Gubbins, D. (1977). Energetics of the Earth's core. *Journal of Geophysics*, *43*, 453–464.

Gubbins, D., Sreenivasan, B., Mound, J., & Rost, S. (2011). Melting of Earth's inner core. *Nature*, *473*(7347), 361–363. https://doi.org/10.1038/nature10068

Hill, R. (1952). The elastic behavior of a crystalline aggregate. *Proceedings of the Physical Society, Section A*, *65*(5), 349–355. https://doi.org/10.1088/0370-1298/65/5/307

Huang, H. H., Lin, F. C., Tsai, V. C., & Koper, K. D. (2015). High-resolution probing of inner core structure with seismic interferometry. *Geophysical Research Letters*, *42*, 10622–10630. https://doi.org/10.1002/2015GL066390

Iritani, R., Takeuchi, N., & Kawak, H. (2014). Intricate heterogeneous structures of the top 300 km of the Earth's inner core inferred from global array data: I. Regional 1D attenuation and velocity profiles. *Physics of the Earth and Planetary Interiors*, *230*, 15–27. https://doi.org/10.1016/j.pepi.2014.02.002

Jacobs, J. (1953). The Earth's inner core. *Nature*, *172*(4372), 297–298. https://doi.org/10.1038/172297a0

Jones, C. A. (2000). Convection-driven geodynamo models. *Philosophical Transactions of the Royal Society of London A*, *358*(1768), 873–897. https://doi.org/10.1098/rsta.2000.0565

Karato, S.-I. (1993). Inner core anisotropy due to magnetic field-induced preferred orientation of iron. *Science*, *262*(5140), 1708–1711. https://doi.org/10.1126/science.262.5140.1708

Karato, S.-I. (1999). Seismic anisotropy of the Earth's inner core resulting from flow induced by Maxwell stresses. *Nature*, *402*, 871–873. https://doi.org/10.1038/47235

Kennett, B. L. N., Engdahl, E. R., & Buland, R. (1995). Constraints on the velocity structure in the Earth from travel times. *Geophysical Journal International*, *122*(1), 108–124. https://doi.org/10.1111/j.1365-246X.1995.tb03540.x

Labrosse, S., Poirier, P., & Mouël, J. L. L. (2001). The age of the inner core. *Earth and Planetary Science Letters*, *190*(3–4), 111–123. https://doi.org/10.1016/S0012-821X(01)00387-9

Lasbleis, M., Deguen, R., Cardin, P., & Labrosse, S. (2015). Earth's inner core dynamics induced by the Lorentz force. *Geophysical Journal International*, *202*(1), 548–563. https://doi.org/10.1093/gji/ggv155

Leykam, D., Tkalčić, H., & Reading, A. M. (2010). Core structure re-examined using new teleseismic data recorded in Antarctica: Evidence for, at most, weak cylindrical seismic anisotropy in the inner core. *Geophysical Journal International*, *180*(3), 1329–1343. https://doi.org/10.1111/j.1365-246X.2010.04488.x

Lincot, A., Merkel, S., & Cardin, P. (2015). Is inner core seismic anisotropy a marker for plastic flow of cubic iron? *Geophysical Research Letters*, *42,* 1326–1333. https://doi.org/10.1002/2014GL062862

Loper, D. E. (1978). Gravitationally powered dynamo. *Geophysical Journal International*, *54*(2), 389–404. https://doi.org/10.1111/j.1365-246X.1978.tb04265.x

Mattesini, M., Belonoshko, A. B., Buforn, E., Ramírez, M., Simak, S. I., Udías, A., . . . & Ahuja, R. (2010). Hemispherical anisotropic patterns of the Earth's inner core. *Proceedings of the National Academy of Sciences of the United States of America*, *107*(21), 9507–9512. https://doi.org/10.1073/pnas.1004856107

Mattesini, M., Belonoshko, A. B., Tkalčić, H., Buforn, E., Udías, A., & Ahuja, R. (2013). Candy wrapper for the Earth's inner core. *Scientific Reports*, *3*, 2096–2103. https://doi.org/10.1038/srep02096

Mizzon, H., & Monnereau, M. (2013). Implication of the lopsided growth for the viscosity of Earth's inner core. *Earth and Planetary Science Letters*, *361*, 391–401. https://doi.org/10.1016/j.epsl.2012.11.005

Monnereau, M., Calvet, M., Margerin, L., & Souriau, A. (2010). Lopsided growth of Earth's inner core. *Science*, *328*(5981), 1014–1017. https://doi.org/10.1126/science.1186212

Morelli, A., Dziewonski, A. M., & Woodhouse, J. H. (1986). Anisotropy of the inner core inferred from PKIKP travel times. *Geophysical Research Letters*, *13*(13), 1545–1548. https://doi.org/10.1029/GL013i013p01545

Niu, F., & Wen, L. (2001). Hemispherical variations in seismic velocity at the top of the Earth's inner core. *Nature*, *410*, 1081–1084. https://doi.org/10.1038/35074073

Olson, P., & Deguen, R. (2012). Eccentricity of the geomagnetic dipole caused by lopsided inner core growth. *Nature Geoscience*, *5*(8), 565–569. https://doi.org/10.1038/NGEO1506

Pejić, T., Tkalčić, H., Sambridge, M., Cormier, V. F., & Benavente, R. (2017). Attenuation tomography of the upper inner core. *Journal of Geophysical Research: Solid Earth*, *122*, 3008–3032. https://doi.org/10.1002/2016JB013692

Romanowicz, B., Cao, A., Godwal, B., Wenk, R., Ventosa, S., & Jeanloz, R. (2016). Seismic anisotropy in the Earth's innermost inner core: Testing structural models against mineral physics predictions. *Geophysical Research Letters*, *43,* 93–100. https://doi.org/10.1002/2016JB013692

Romanowicz, B., Tkalčič, H., & Bréger, L. (2003). On the origin of complexity in Pkp travel time data. In V. Dehant, K. C. Creager, S.-I. Karato & S. Zatman (Eds.), *Earth's core: Dynamics, structure, rotation*. Washington, DC: American Geophysical Union. https://doi.org/10.1029/GD031p0031

Ruban, A. V., Belonoshko, A. B., & Skorodumova, N. V. (2013). Impact of magnetism on Fe under Earth's core conditions. *Physical Review B*, *87*(1), 014405–014411. https://doi.org/10.1103/PhysRevB.87.014405

Shearer, P. M. (1994). Constraints on inner core anisotropy from PKP(DF) travel times. *Journal of Geophysical Research: Solid Earth*, *99*(B10), 19647–19659. https://doi.org/10.1029/94JB01470

Shearer, P. M., & Toy, K. M. (1991). PKP(BC) versus PKP(DF) differential travel times and aspherical structure in the Earth's inner core. *Journal of Geophysical Research: Solid Earth*, *96*(B2), 2233–2247. https://doi.org/10.1029/90JB02370

Song, X. (1997). Anisotropy of the Earth's inner core. *Reviews of Geophysics*, *35*(3), 297–313. https://doi.org/10.1029/97RG01285

Stixrude, L., & Cohen, R. E. (1995). High-pressure elasticity of iron and anisotropy of Earth's inner core. *Science*, *267*(5206), 1972–1975. https://doi.org/10.1126/science.267.5206.1972

Sumita, I., & Olson, P. (1999). A laboratory model for convection in Earth's core driven by a thermally heterogeneous mantle. *Science*, *286*(5444), 1547–1549. https://doi.org/10.1126/science.286.5444.1547

Tanaka, S., & Hamaguchi, H. (1997). Degree one heterogeneity and hemispherical variation of anisotropy in the inner core from PKP(BC)-PKP(DF) times. *Journal of Geophysical Research: Solid Earth*, *102*(B2), 2925–2938. https://doi.org/10.1029/96JB03187

Thomsen, L. (1986). Weak elastic-anisotropy. *Geophysics*, *51*(10), 1954–1966. https://doi.org/10.1190/1.1442051

Tkalčić, H. (2010). Large variations in travel times of mantle-sensitive seismic waves from South Sandwich Islands: Is the Earth's inner core a conglomerate of anisotropic domains. *Geophysical Research Letters*, *37*, L14312. https://doi.org/10.1029/2010GL043841

Tkalčić, H. (2015). Complex inner core of the Earth: The last frontier of the global seismology. *Reviews of Geophysics*, *53*, 1–36. https://doi.org/10.1002/2014RG000469

Tkalčić, H. (2017). *The Earth's inner core*. Cambridge, UK: Cambridge University Press.

Tkalčić, H., Romanowicz, B., & Houy, N. (2002). Constraints on D'' structure using PKP(AB-DF), PKP(BC-DF) and PcP-P traveltime data from broad-band records. *Geophysical Journal International*, *149*(3), 599–616. https://doi.org/10.1046/j.1365-246X.2002.01603.x

Tkalčić, H., Young, M., Muir, J. B., Davies, D. R., & Mattesini, M. (2015). Strong, multi-scale heterogeneity in Earth's lowermost mantle. *Scientific Reports*, *5*, 18416. https://doi.org/10.1038/srep18416

Turcotte, D. L., & Schubert, G. (2002). *Geodynamics* (2nd ed.). Cambridge, UK, Cambridge University Press.

Verhoogen, J. (1961). Heat balance of the Earth's core. *Geophysical Journal of Royal Astronomical Society*, *4*(s0), 276–291. https://doi.org/10.1111/j.1365-246X.1961.tb06819.x

Wu, W., & Irving, J. C. E. (2017). Using PKiKP coda to study heterogeneity in the top layer of the inner core's western hemisphere. *Geophysical Journal International*, *209*(2), 672–687. https://doi.org/10.1093/gji/ggx047

Yee, T.-G., Rhie, J., & Tkalčić, H. (2014). Regionally heterogeneous uppermost inner core observed with Hi-net array. *Journal of Geophysical Research: Solid Earth*, *119*, 7823–7845. https://doi.org/10.1002/2014JB011341

Yoshida, S., Sumita, I., & Kumazawa, M. (1996). Growth model of the inner core coupled with the outer core dynamics and the resulting elastic anisotropy. *Journal of Geophysical Research: Solid Earth*, *101*(B12), 28085–28103. https://doi.org/10.1029/96JB02700

Young, M. K., Tkalčić, H., Bodin, T., & Sambridge, M. (2013). Global P-wave tomography of Earth's lowermost mantle from partition modeling. *Journal of Geophysical Research: Solid Earth*, *118*, 5467–5486. https://doi.org/10.1002/jgrb.50391